communications earth & environment

A Nature Portfolio journal

Article

https://doi.org/10.1038/s43247-025-02113-7

Variable fault geometry controls the cascading 2023 Herat, Afghanistan multiplet sequence

Lei Zhao[1,2], Edwin Nissen[2,3], Wenbin Xu[1] ✉, Mohammadreza Jamalreyhani[4], Eric A. Bergman[5], Dezheng Zhao[6] & Lei Xie[1]

Earthquake multiplets are an important but poorly understood class of seismic sequence. On October 7th–15th 2023, a multiplet comprising five damaging, moment magnitude (M_w) 5.9–6.4 earthquakes struck northwestern Afghanistan, a region previously lacking in well-recorded seismicity. We mapped ground deformation with Interferometric Synthetic Aperture Radar (InSAR) and characterized the causative faulting using elastic dislocation modelling. Because of the tight clustering in time, only the fifth mainshock is ever imaged on its own, so we apply independent seismological constraints from epicentral relocations and moment tensor inversions to distinguish the contribution of each mainshock to the observed surface deformation. Our results support sequential rupture of five colinear, shallow (~5 km), north-dipping, blind reverse faults, with successive mainshocks stepping initially westwards and subsequently eastwards. Our modelling implies that gentle (10–15°) fault bends and/or step-overs may have halted rupture propagation in individual mainshock, acting to divide the sequence into its five distinct events. The epicentral region shows abundant geomorphic evidence for active shortening, including a ~70 km-long anticlinal ridge whose growth is likely driven by the underlying reverse faults. This sequence confirms that while to a first degree northwestern Afghanistan is part of stable Eurasia, slow internal deformation can nevertheless generate damaging earthquakes.

Multiplet earthquake sequences are those dominated by two or more distinct mainshock events, separated by periods ranging from a few seconds up to several years. In addition to the additive hazards that they entail, multiplets pose methodological challenges to seismic hazard analyses and operational earthquake forecasting, challenging the basic assumption of quasi-periodic earthquake recurrence and raising the spectre that the hazard following a mainshock event may go up, rather than down[1]. Those that rupture in quick succession can also be complicated to interpret, generating overlapping surface deformation signals and, at the shortest intervals, concurrent seismic wave trains[2–8]. However, when carefully characterized, multiplets can offer valuable insights into earthquake processes such as rupture nucleation, propagation, and arrest, static and dynamic stress triggering, and other mechanisms of fault interaction. In recent decades, several notable examples have involved reverse faulting within fold-and-thrust belts, most numerously in the Zagros mountains of southern Iran[8–18] but also in the mountains of Kerman Province in central Iran[19], the Afghan-Tajik depression[20], the Sulaiman ranges in Pakistan[7,21], the Kepintag and North Qaidam thrust systems in western China[22,23], and the Mackenzie mountains in Canada[24]. Given their apparent frequency in these settings, it is important to understand whether the sequences share common characteristics and mechanisms.

Over the span of a few days in October 2023, five damaging earthquakes struck near the city of Herat in northwestern Afghanistan (Fig. 1a), killing nearly 1500 people and destroying more than 10,000 homes according to the World Health Organization. The quintuplet comprised two M_w 6.2–6.3 earthquakes on October 7th, only 32 min apart (hereafter 'EQ1' and 'EQ2'), followed 28 min later by a M_w 5.8–5.9 earthquake ('EQ3'); a M_w 6.2–6.3 earthquake on October 11th ('EQ4'); and a M_w 6.3–6.4 earthquake on October 15th ('EQ5') (Fig. 1b). The United States Geological Survey Comprehensive Earthquake Catalog (USGS ComCat) places these earthquakes within 20 km of one another; similar to likely uncertainties in individual catalog epicenters[25] and rendering exact spatial relations obscure.

[1]School of Geoscience and Info-Physics, Central South University, Changsha, China. [2]School of Earth and Ocean Sciences, University of Victoria, Victoria, BC, Canada. [3]College of Earth, Ocean and Atmospheric Sciences, Oregon State University, Corvallis, OR, USA. [4]Department of Earth and Space Sciences, Southern University of Science and Technology, Shenzhen, China. [5]Global Seismological Services, Golden, CO, USA. [6]State Key Laboratory for Mineral Deposits Research, School of Earth Sciences and Engineering, Nanjing University, Nanjing, China. ✉e-mail: wenbin.xu@csu.edu.cn

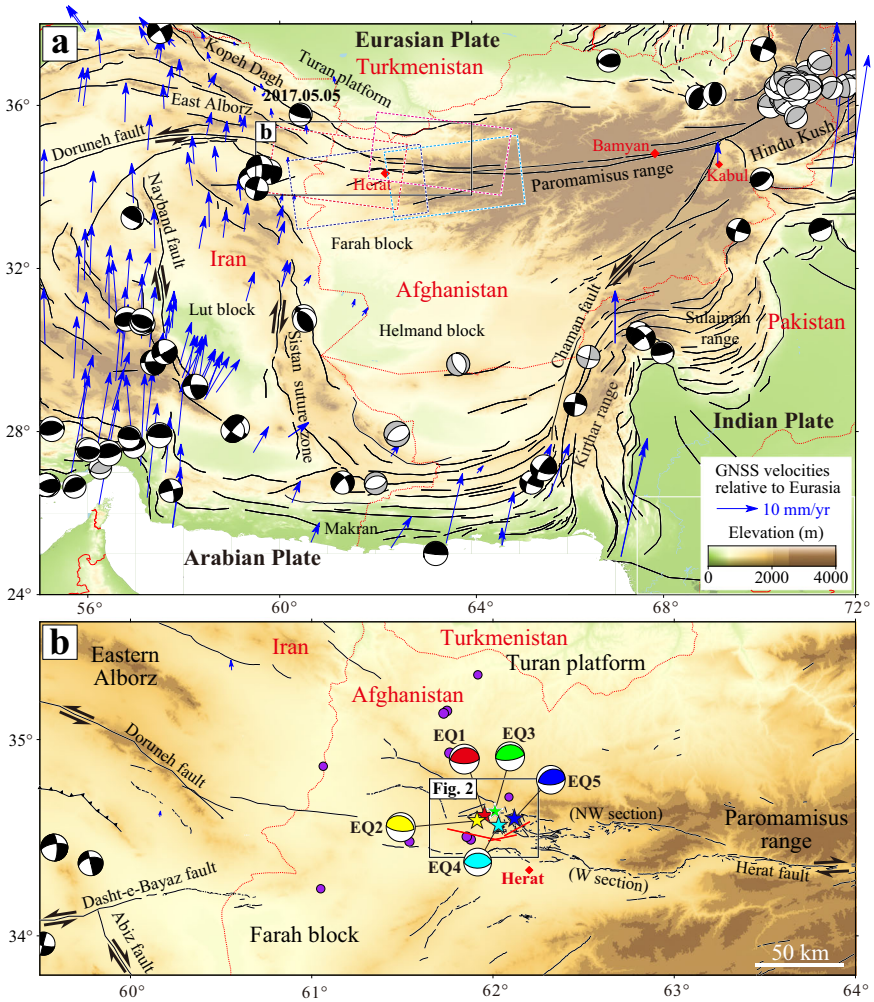

Fig. 1 | Tectonic setting of Afghanistan. a Focal mechanisms of $M_w > 6$ earthquakes from 1900 to 2022 are taken from the USGS ANSS Comprehensive Earthquake Catalog (ComCat), with shallow (<30 km) events in black (the one labelled 2017.04.05 is the M_w 6.1 Sefid Sang earthquake[77], referred to in Methods) and deep (> 30 km) ones in grey. Black lines are active faults from the Global Earthquake Model (GEM)[92]. Carmine and light blue rectangles indicate the Sentinel-1 SAR scenes used in this study. Blue arrows are interseismic GNSS velocities in a stable Eurasia reference frame[64,93]. Red diamonds are the main cities. The black rectangle shows coverage of (**b**). **b** Regional setting with faults from the USGS[46]. Colored stars and beach balls are USGS epicenters and W-phase focal mechanisms of the five 2023 Herat mainshocks, and red lines are surface projections of our initial InSAR model faults.

Automated source mechanisms from the USGS, Global Centroid Moment Tensor (GCMT) and GEOFON catalogs show that each of the earthquakes involved reverse faulting on nodal planes trending roughly E-W and dipping at moderate angles of ~45° ± 20° (Table S1). Automated centroid depths (4–17 km) imply upper crustal faulting, but these catalogs are usually unable to refine this parameter with any more precision[26–29]. According to the USGS ComCat, the sequence also includes seventeen smaller earthquakes of M_w 4.5–5.4 up to October 28th 2023. The Herat sequence thus provides a rich dataset for learning more about the mechanics of multiplet earthquakes in thrust belt settings.

Since they are also the first instrumentally well-recorded, large earthquakes in central or western Afghanistan—an area completely lacking in either Global Navigation Satellite System (GNSS) velocities or robust fault slip rate data—the 2023 Herat quadruplet sequence also offers valuable insights into regional tectonics. Afghanistan lies between three major plate boundary systems (Fig. 1a). To the south, Arabian oceanic lithosphere subducts northwards at ~30 mm/yr beneath the Makran accretionary prism, generating intermediate depth (up to ~150 km) seismicity along Afghanistan's southern border at ~30° N[30]. To the west, in eastern Iran, the N-S trending, right-lateral Nayband and Sistan faults and the conjugate, left-lateral Dasht-e-Bayaz and Doruneh faults together accommodate ~15 mm/yr of northward motion of central Iran with respect to Eurasia[31,32]. To the east, the NNE-trending, left-lateral Chaman fault in eastern Afghanistan and the Kirthar and Sulaiman ranges in neighboring Pakistan accommodate ~30 mm/yr of northward motion of the Indian continent[33–35], while localized subduction is manifest in intermediate depth (up to ~250 km) earthquakes beneath the Hindu Kush in northeastern Afghanistan[36]. This eastern tectonic boundary is responsible for the great majority of recorded seismicity in Afghanistan[37]. In the absence of an obviously active fault system in the north, and given its sparse instrumental seismicity and relatively gentle topographic relief, the intervening region of central and western Afghanistan is often considered a southern promontory of the stable Eurasia plate[38,39].

The most likely candidate for an active fault in this region is the right-lateral Herat (or Hari Rud) fault, which strikes ~E-W for ~700 km across northern Afghanistan, from its intersection with the Chaman fault north of Kabul in the east to close to the Iranian border in the west[40–42] (Fig. 1a). According to historical records, the city of Herat, along the western part of the fault, was impacted by earthquakes in AD 847, 1102, 1364, 1908, 1931 and 1950, while the Bamyan district, on the eastern part of the fault, was widely damaged in a M 7.4 earthquake in 1950, though this likely occurred on a neighboring, NE-trending structure[37,43,44]. The Herat fault follows the early Jurassic suture of the Farah block, a fragment of Gondwana, to the Turan (Northern Afghan) platform, which marks the southern margin of Laurasia[42,45]. Regional shortening continued during the late Jurassic and early Cretaceous driven by the accretion of a second Gondawan terrane, the Helmand block, to the south. Subsequent Cenozoic right-lateral slip on the Herat fault was driven by the westward, lateral extrusion of central Afghanistan out of the way of the India-Eurasia collision[42]. Narrow pull-apart basins filled with Oligo-Miocene sediment suggests that strike-slip motion peaked at this time, while numerous, smaller geomorphic offsets of tens to hundreds of meters attest to continued, but likely slower, activity during the Quaternary[46,47]. Sborshchikov et al.[41] estimated a Quaternary slip rate of ~2 mm/yr based on assigning 5 km-wide drainage offsets an age of 2 Myr, but more precise determinations based on dated rocks or landforms are currently lacking.

For much of its length the Herat fault closely parallels the Hari river (Harī Rōd), but west of 63.3° E it bifurcates into two main strands, one in the south following the southern margin of the Paropamisus mountains (Selseleh-ye Safīd Kūh), and the other following parallel sub-ranges to the north[46,47] (Fig. 1b). The USGS have termed these the western (W) and northwestern (NW) sections, respectively. The October 2023 earthquake sequence occurred between these two strands, in a basin containing incised Miocene, Pliocene and Pleistocene clastic sediments and crossed by an abundance of shorter, secondary faults[46,48]. The two strands project westwards towards SE-trending ranges of the easternmost Alborz in eastern Iran, but both appear to die out short of the border.

In this paper, we carefully characterize the 2023 Herat quintuplet earthquakes using the best available geodetic and seismological data. We use InSAR measurements derived from 11 independent Sentinel-1 SAR scenes coupled with Bayesian inversion methods to solve for the best fitting fault geometries and slip distributions. These models are then checked and revised using independent seismological constraints from calibrated hypocentral relocations and teleseismic and regional waveform models. We finish by discussing implications for the mechanics of multiplet sequences in reverse faulting settings, whether there is a geomorphic signature to the causative faulting in the landscape, and how the Herat sequence helps illuminate the active tectonics of western Afghanistan.

Results

Coseismic deformation

We mapped coseismic surface deformation in the 2023 Herat earthquake sequence using seven interferograms constructed from eleven individual Sentinel-1A scenes captured from two ascending and two descending tracks (see Methods). The four descending and three ascending interferograms each exhibit roughly elliptical patterns of deformation toward the satellite, bordered in some cases by subtle, longer wavelength displacements away from the satellite (Fig. 2a–f and Supplementary Fig. S1). The absence of any sharp discontinuities between deformation toward and away from the satellite is characteristic of buried reverse faulting[8–12]. Because the 12 day Sentinel-1A revisit time greatly exceeds the ≤ 4 day intervals between successive mainshocks, most of the interferograms capture multiple mainshocks (Fig. 2m). The fullest spatial coverage of the sequence is provided by ascending track A13 and descending track D20. Here, EQ1, EQ2, and EQ3 are imaged together as an elongated (~25 km × 5 km), ESE-WNW-trending deformation pattern with peak displacements of ~0.4–0.6 m (Fig. 2g, h). The subsequent acquisitions on tracks A13 and D20 capture EQ4 and EQ5 as an elongated (~15 km × 5 km), ENE-trending deformation zone with peak displacements of ~0.6–0.8 m, centered east of the main EQ1–EQ3 signal (Fig. 2j, k). The main fringe ellipse is bordered to the south by a long, narrow, ~E-W trending uplift signal with maximum displacement of ~0.2 m (Fig. 2d–f), which is colocated with the straight southern edge of the earlier EQ1–EQ3 fringe ellipse (Fig. 2a–c). The adjacent ascending track A115 and descending track D122 capture only the eastern part of the deforming area. One pair of A115 and D122 interferograms capture EQ1–EQ3 together with EQ4 (Fig. 2i and Fig. S2). EQ5 is the only earthquake to be imaged solitarily, in a single descending track D122 interferogram containing a smaller (~10 km × 5 km) deformation pattern with peak displacement of ~0.6 m, centered east of the signals from EQ1–EQ4 (Fig. 2l).

InSAR slip modelling

We first modelled EQ1, EQ2 and EQ3 using uniformly downsampled data[49] from the interferograms in Fig. 2a, b, having found that a conventional quadtree decomposition[49] undersampled the longer-wavelength deformation lobes. In our initial non-linear inversion for fault geometry (see Methods), we found that a single, north-dipping fault plane can fit the data reasonably well, with a narrow peak in each posterior probability distribution indicating a tightly-constrained uniform slip solution (Fig. S3). For our subsequent linear inversion for the slip distribution on this plane, a smoothing factor of 0.03 was selected after using the L-curve to minimize residuals without overfitting[50] (Fig. S2). The resulting model interferogram matches the data well, with residuals of up to 5 cm (Fig. S4c, S4f). Model slip is distributed across a ~20 km × 5 km fault patch, consistent with the elongate pattern observed in the interferograms, with peak slip of ~1.1 m occurring at a depth of 5–6 km (Fig. 3a). The model moment of 6.5×10^{18} Nm (equivalent to M_w 6.5) is similar to the sum of the seismological moments of EQ1, EQ2 and EQ3 (Table S1), indicating that the model captures all three earthquakes. However, while the optimal strike of ~281.5° and northward dip of ~38° closely match the WNW-striking nodal planes of the available seismological solutions for EQ2, they are misaligned with the WSW-striking nodal planes of EQ1 and EQ3. This hints that our simple, one fault model and its smooth slip distribution may mask additional fault complexity, a point we revisit by incorporating seismological constraints.

Considering that EQ4 is only imaged together with either EQ1–EQ3 (Fig. 2c and S2) or EQ5 (Fig. 2d, e), we considered EQ5 next, modelling it using uniformly downsampled data from the descending interferogram in Fig. 2f. The nonlinear inversion results in a best-fitting fault strike of ~243°, dip of ~36.5°, and rake of ~71° (Fig. S5). These parameters lie within a few degrees of the WSW-striking nodal planes of the seismological models (Fig. 3a), suggesting that our reliance upon a single InSAR look-angle has not proven problematic. The linear inversion yields an elliptical, ~10 km × 5 km slip patch with maximum slip of ~2.35 m at ~4 km depth (Fig. 3a). The model moment of 3.2×10^{18} Nm closely matches seismological estimates (Table S1) and the RMS of the residuals is ~1.2 cm, indicating that the simulated data fit the observations well (Fig. 4p–r).

To determine the fault geometry of EQ4, we first removed the deformation contributions predicted by our best-fitting models of EQ1, EQ2, EQ3, and EQ5 from the interferograms in Fig. 2c, d, e, yielding residual interferograms that should contain only EQ4 (Fig. 4g, j, m). These were then downsampled and inverted in the usual way. The nonlinear inversion yields an optimal strike of ~259° and dip of ~36.5° (Fig. S7), consistent with the northward dipping nodal planes of the seismological EQ4 models (Fig. 5). The linear inversion suggests that the coseismic slip is distributed across an elliptical fault patch of ~10 km × 5 km, with peak slip of ~2.5 m at ~5.1 km depth (Fig. 3a). We acknowledge several residual fringes, especially at the southern (up-dip) edge of the fringe ellipse, but these are inevitable due to our corrections for EQ1-EQ3 and EQ5 being applied to interferograms spanning a mix of acquisition dates (Fig. 4g–o). The model moment of 6.2×10^{18} Nm (equivalent to M_w 6.5) is at least twice any of the seismological estimates, implying that our model incorporates some aseismic afterslip, though we note that there are also significant uncertainties in seismological moment from its known trade-off against centroid depth.

Our InSAR modelling thus supports sequential rupture of at least three discrete reverse faults or fault segments (red lines in Fig. 1b), each dipping northward at ~37° but whose strikes curve from ~WNW in the west (in EQ1–EQ3) through ~W centrally (in EQ4) to ~WSW in the east (in EQ5). EQ1, EQ2 and EQ3 cannot be distinguished from the InSAR data alone, and are fit reasonably well by a continuous, ~20 km-long slip patch on a single fault plane, while EQ4 and EQ5 are each shorter at ~10 km-long (Fig. 3). Rupture in all five events is buried at depths of ~2–8 km, peaking at ~4–6 km. In the following section, we further test these interpretations using independent seismological data.

Multiple-event hypocentral relocations

We relocated epicenters of the Herat sequence using arrival times from regional Iranian and teleseismic stations (see Methods). The relocated epicenters of EQ1–EQ3 and EQ4 lie centrally within their corresponding InSAR deformation patches (Fig. 2a–e), confirming our interpretations from InSAR modelling and justifying our approach to performing the direct calibration with data relatively far from the events of interest and relying on far regional and teleseismic data to provide the needed connectivity for accurate relative locations. Following EQ1, the sequence propagated along strike in both directions, first westwards in EQ2, and then progressively eastwards in EQ3, EQ4 and EQ5. This pattern is also evident in the migration of smaller aftershocks (Fig. 3c).

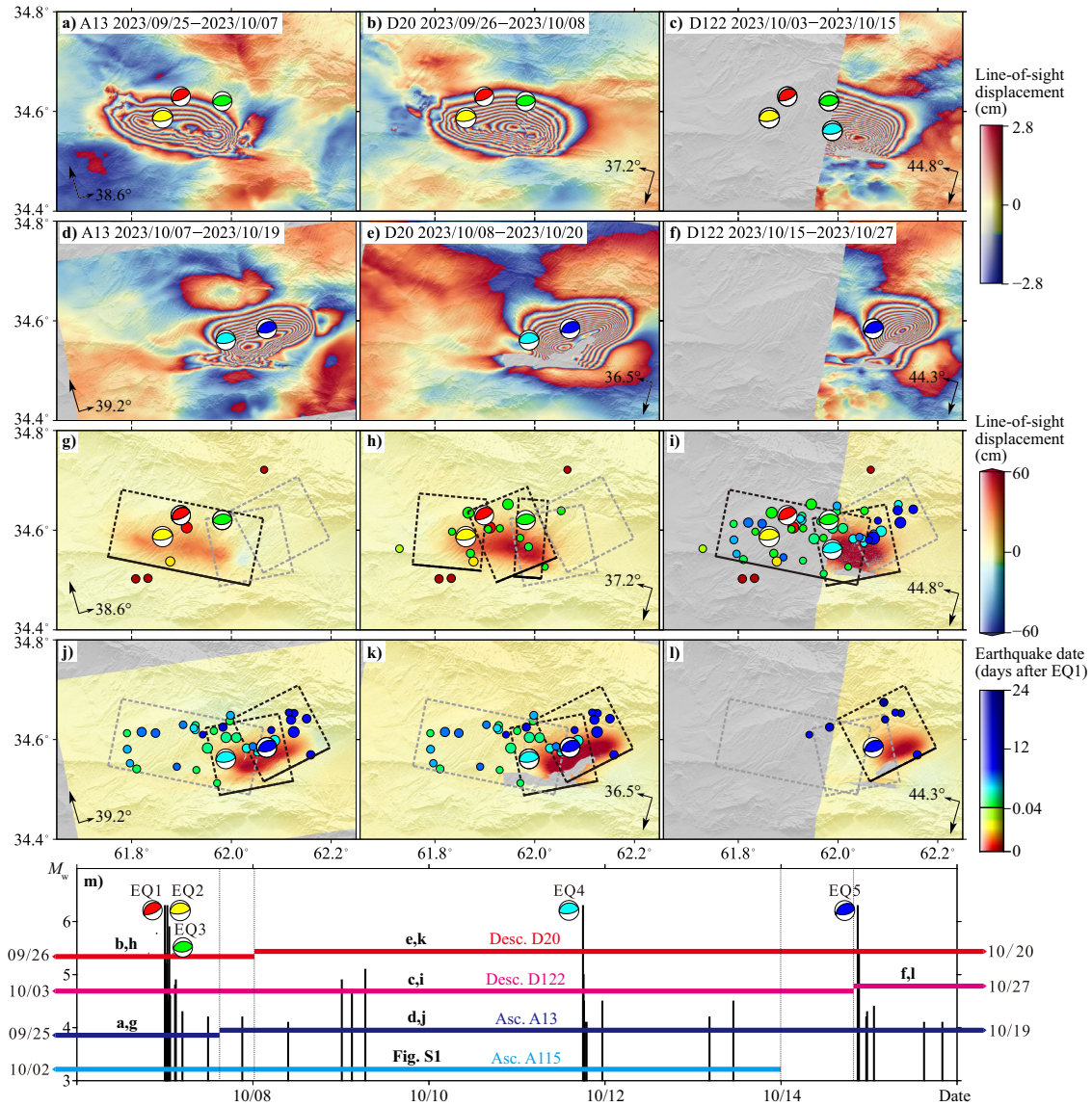

Fig. 2 | Coseismic deformation field of the 2023 Herat sequence. Wrapped (**a**–**f**) and unwrapped (**g**–**l**) coseismic interferograms capturing various stages of the 2023 Herat sequence (see Table S2 for details). Colored beach balls are USGS W-phase focal mechanisms at relocated epicenters for the captured mainshock(s). In (**g**–**l**), rectangles are northward dipping InSAR model fault planes, with those highlighted in black interpreted to be contributing towards the observed deformation. Satellite azimuth and line-of-sight directions are labelled with the incidence angle measured at the maximum coseismic displacement. Small circles are relocated aftershocks spanned by the interferogram in question, colored by days after EQ1. **a**, **g** Ascending track A13 interferogram spanning EQ1, EQ2 and EQ3. **b**, **h** Descending track D20 interferogram spanning EQ1, EQ2 and EQ3. **c**, **i** Descending track D122 interferogram spanning EQ1, EQ2, EQ3 and EQ4. **d**, **j** Ascending track A13 interferogram spanning EQ4 and EQ5. **e**, **k** Descending track D20 interferogram spanning EQ4 and EQ5. **f**, **l** Descending track D122 interferogram spanning EQ5. **m** Temporal baseline of the seven interferometric pairs (horizontal lines) and recorded earthquakes (vertical lines, scaled by magnitude).

Seismic moment tensor inversion

We calculated the focal mechanisms of the five mainshock events using high signal-to-noise ratio seismic records at both teleseismic and regional distances (see Methods). This approach refines estimates of source parameters from those listed in the USGS, GCMT and GEOFON catalogs, particularly centroid depth which is often fixed for the automated solutions[26–29]. Our enforced double couple (DC) solutions show pronounced variations in the trend of the N-dipping nodal planes, with EQ1 and EQ5 striking ~WSW and EQ2–EQ4 striking ~W, relative differences also observed in the USGS, GCMT, and GEOFON mechanisms (Fig. 5 and Table S1). Our N-dipping DC nodal planes are generally in close agreement with our InSAR model fault planes, with discrepancies in strike, dip and rake of mostly just a few degrees and always less than 20°, thus lying within typical uncertainties for waveform inversions of thrust earthquakes[11,26]. Our DC centroid depths are also in very close agreement with the InSAR slip models for EQ2 and EQ3, but a few kilometers deeper (at 9–10 km) for EQ1, EQ4, and EQ5.

To explore uncertainties in centroid depth further, we relaxed the double couple requirement and solved for the non-double couple (non-DC) moment tensors (see Methods). Freeing up parameter space in this way does not significantly improve the visual fit to the waveforms over the DC models (Figs. S8–S9), but does result in quicker convergence into stable solutions, reflected in well-defined fuzzy moment tensors (Fig. 6a), narrow, single peaks in the centroid depth probability distribution function (Fig. 6b-c), and smooth bootstrap optimization curves (Fig. 6d). For EQ2 and EQ3, non-DC moment tensors retain the shallow (4–5 km) centroid depths of the DC mechanisms, indicating tightly-constrained depths in close agreement with the InSAR slip models (~4 km). For EQ1, EQ4 and EQ5, non-DC moment tensors are significantly shallower than the DC solutions (at 4–6 km versus

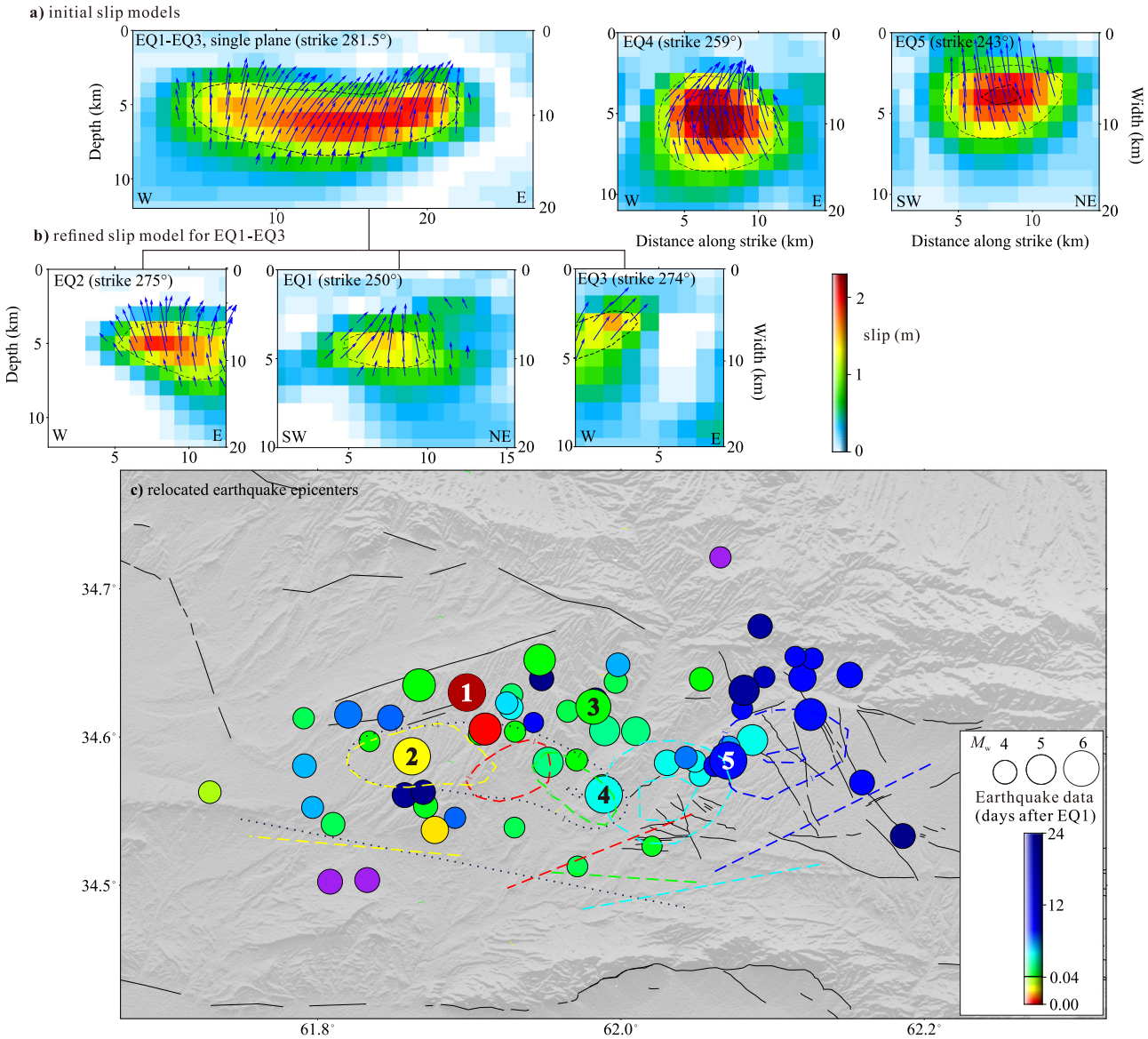

Fig. 3 | Slip distribution of the 2023 Herat sequence. a InSAR model slip distributions of (left) EQ1, EQ2 and EQ3, assuming a single fault plane, (center) EQ4, and (right) EQ5. Blue arrows show movement of the hanging wall with respect to the footwall, and slip contours are at increments of 1 m. **b** Refined model slip distribution for EQ1, EQ2 and EQ3, assuming separate fault planes. **c** Relocated epicenters coloured by event date (relative to EQ1). Ellipses show the same coseismic slip contours of EQ1–EQ3 (black, single fault model), EQ1 (red), EQ2 (yellow), EQ3 (green), EQ4 (cyan), and EQ5 (blue); coloured straight lines are the model fault surface projections. Black lines are mapped surface faults from the USGS[46].

9–10 km), indicating uncertainties of a few kilometers in centroid depth, as is typical for this approach[26–29]. The shallow end of this acceptable centroid depth range is in close agreement with the InSAR slip models (Fig. 5 and Table S1). Compensated linear vector dipole (CLVD) components of 20–40% are similar to those resolved independently by the USGS, GCMT, and GEOFON, and could be explained by a more complex fault geometry than is resolved by the InSAR data[51]. However, the strikes, dips, and rakes of the best double couple approximations to our non-DC solutions vary little from the earlier, DC solutions (Fig. 5 and Table S1), which suggests that the overall geometry is unchanged.

The seismology thus supports our interpretation of the InSAR that the Herat mainshocks progressed bilaterally along strike at first, and then unilaterally eastwards, along fault segments that rotate from more westerly trends in the west (in particular in EQ2) to more south-westerly trends in the east (in EQ5). The spatial and geometric relationship between EQ1, EQ2 and EQ3 remains obscure, though they nucleated in close proximity (within about 10 km of one another) and are misaligned by ~30° in strike. The shallow (~4–6 km) center depths of the InSAR-derived slip distributions are in close agreement (EQ2 and EQ3) or within error (EQ1, EQ4 and EQ5) to centroid depths from waveform modelling.

A seismologically-informed InSAR slip model for EQ1-EQ3 and further refinements to EQ4 and EQ5

Our preferred, non-DC waveform models contain differences in strike of ~28° between EQ1 and EQ2 and ~26° between EQ1 and EQ3, similar to variations in the respective USGS, GCMT and GEOFON models (Table S1 and Fig. 3). This implies that our initial InSAR model for these three earthquakes, involving a smooth slip distribution on a single fault plane (Fig. 3a), is overly simplistic. To distinguish the separate contributions of the three earthquakes, we therefore assembled multi-fault models that are more consistent with the available seismological data (Table S1). Since EQ1 and EQ2 have two to three times the seismic moment of EQ3, we began with a two fault model. We took the average strike and dip values of the

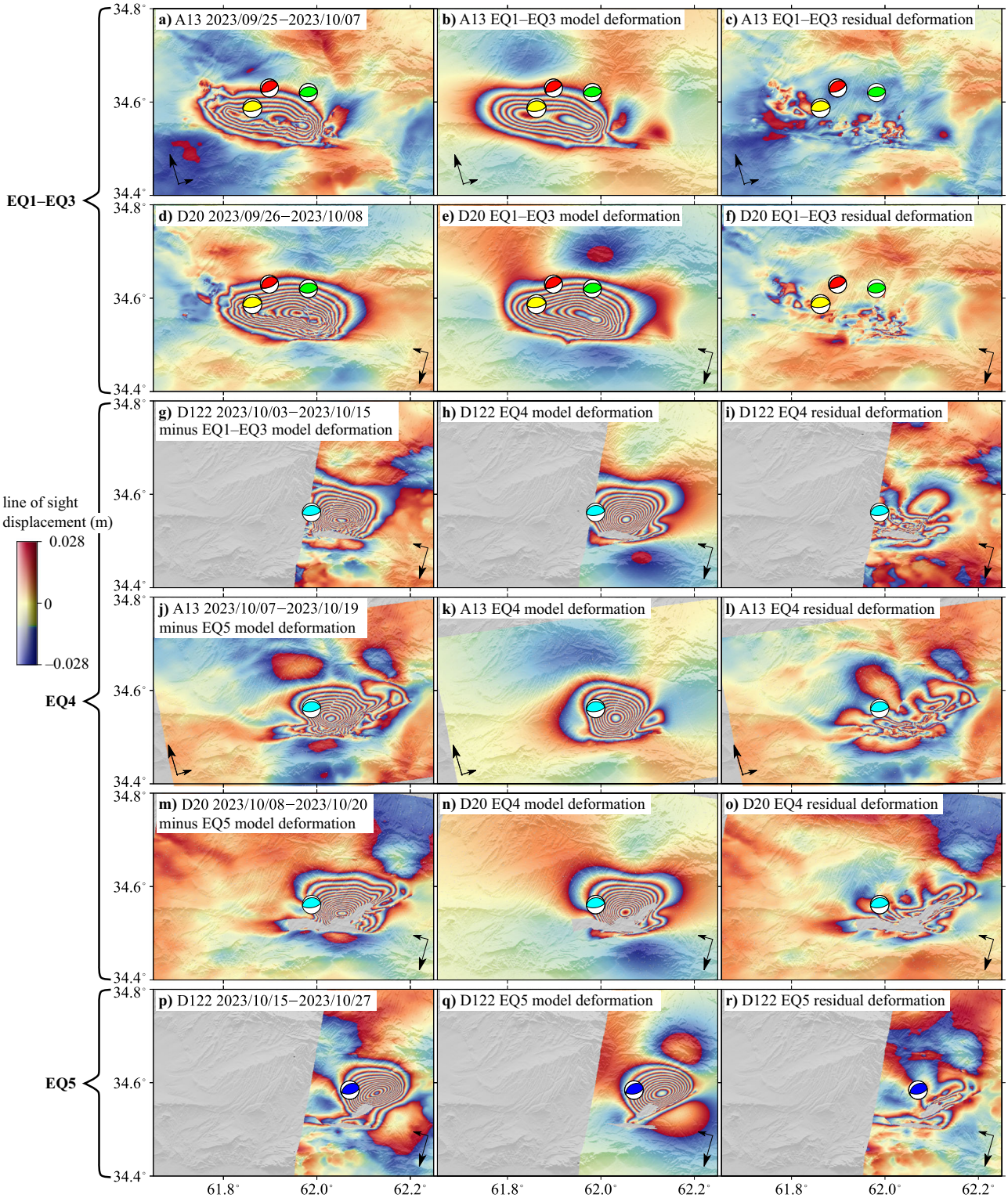

Fig. 4 | InSAR observations, best fitting models and residuals. (Left) Observed, (center) modelled, and (right) residual wrapped interferograms for (top two rows) EQ1–EQ3, (third to fifth rows) EQ4, and (final row) EQ5. The EQ1–EQ3 model and residual interferograms in (**b**, **c**) and (**e**, **f**) are for our preferred three fault model. In (**g**), model deformation from EQ1–EQ3 has been removed, leaving only EQ4. In (**j**,**m**), model deformation from EQ5 has been removed, leaving only EQ4.

seismologically-determined fault planes (EQ1: 250°/31°; EQ2: 275°/37°), projected these upwards to the surface from the calibrated hypocenters, and solved simultaneously for the slip distributions on these planes. The linear inversion yields an elliptical, 10 km × 4 km slip patch on the EQ2 fault plane, with peak slip of ~1.66 m at ~5.4 km depth (Fig. S10b), and two elliptical slip regions on the EQ1 fault plane (Fig. S10a), a deeper, 7 km × 4 km patch with a peak slip of ~1.65 m at ~5.1 km depth, and a shallower 3 km × 2 km patch with peak slip of ~1.3 m at ~2.3 km depth. RMS residual displacements for the ascending and descending models reduce from 20.4 mm and 22.7 mm for the initial, single fault model to 14.9 mm and 15 mm for the two fault model. However, the two fault model interferograms fail to match the distinctly linear, ~E-W trending fringe pattern along the southeastern edge of

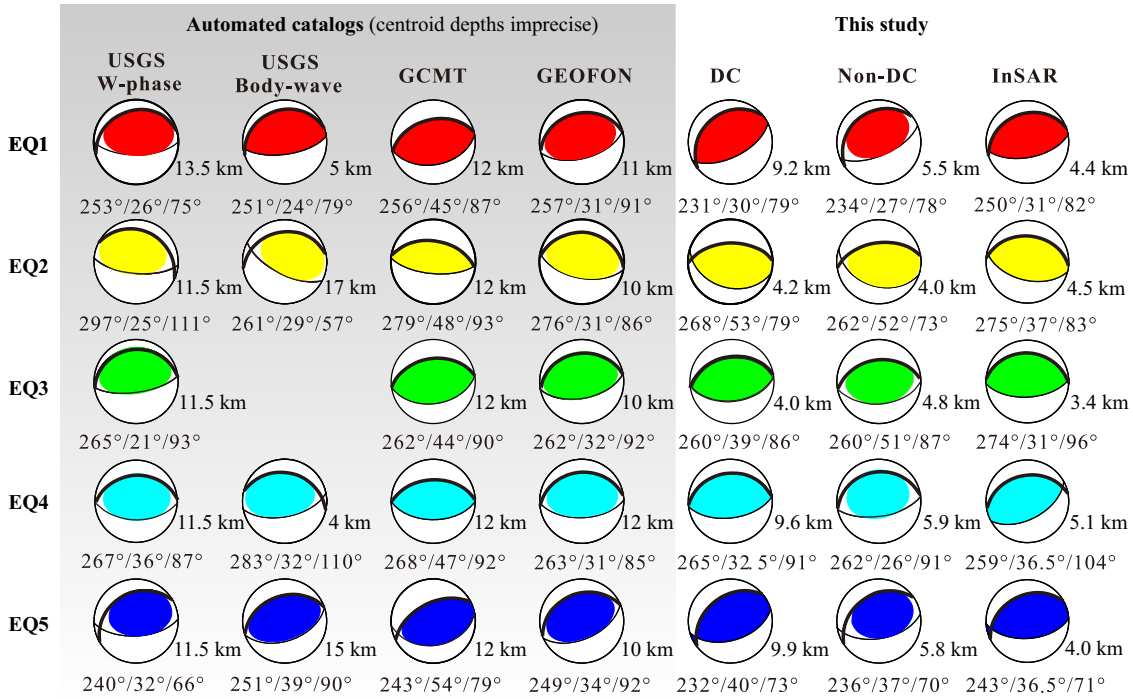

Fig. 5 | Estimated focal mechanisms of the five Herat mainshocks with the interpreted N-dipping fault plane shown in bold and labelled with strike/dip/rake and centroid depth. The first five columns show automated solutions from the USGS W-phase, USGS body wave, GCMT, and GEOFON catalogs; their centroid depths (often fixed) should not be considered robust[26–29]. The sixth to eighth columns show our best double couple (DC) and non-double couple (non-DC) waveform solutions and our InSAR models.

the observed deformation ellipse. As this area is immediately up-dip from the relocated hypocenter of EQ3, we assume a causative link.

We therefore added a third model fault in this area, striking 274° (matching the linear fringe trend and within 9–14° of the seismological nodal planes) and dipping 31° northwards (the average of the seismological nodal planes), and inverted linearly for slip on the three model fault planes together. The modeled data recover the observations well, including in the south-eastern region that was previously poorly fit (Fig. 4a–f), and RMS residuals reduce further to 11.3 mm (ascending) and 11.8 mm (descending). EQ1 now forms a single, elliptical, 8 km × za× h4 km slip patch with peak slip of ~1.5 m at ~4.4 km depth (Fig. 3b). EQ2 still lies west of EQ1, forming a 9 km × 5 km slip patch with peak slip of ~1.9 m at ~4.5 km depth, while EQ3 is narrower (3 km × 2 km), shallower (with peak slip of ~1.51 m at ~3.4 m depth), and to the east of EQ1. InSAR derived moments are ~2.9×10^{18} Nm (equivalent to M_w 6.3), 2.2×10^{18} Nm (equivalent to M_w 6.2), and 1.5×10^{18} Nm (equivalent to M_w 6.1) for EQ1, EQ2 and EQ3 respectively. We acknowledge that the EQ3 InSAR moment is about double that of the seismological values, suggesting some contribution from afterslip driven by EQ3 and/or the proximal parts of nearby EQ1. This is consistent with a narrow deformation pattern observed in later post-seismic imagery (Fig. S11).

Finally, we note that modelled interferograms for EQ4 and EQ5 show narrow, near-field residuals distributed along and directly eastwards of the EQ3 model fault (Fig. 4i, l, o, r). To improve the model fit further, we considered whether shallow afterslip may have occurred along this extended fault plane during the period spanned by the EQ4 and EQ5 interferograms. We extended the EQ3 model fault as far east as the largest aftershock, restricting it to shallow (<2 km) depths to prevent overlap with other fault planes, and then repeated the inversions for EQ4 and EQ5 with added slip on EQ3. Due to masking of the narrow uplift region in the two descending track interferograms, the two fault EQ4 model did not initially improve results much (Fig. S12c, S12f, S12i). However, when only using the ascending data to constrain the two fault model, modelled slip appears on the shallow EQ3 fault, helping recover the narrow deformation signal well and reducing RMS residual displacements from 36.1 mm for a single fault (Fig. 4i) to 25.3 mm for two faults (Fig. S12l). The two fault model for EQ5 also recovers the southern uplift region well, reducing RMS residuals from 16.1 mm for the single fault model to 8.1 mm for the two faults model (Fig. S13). We conclude that the pronounced residuals south of the main EQ4 and EQ5 fringes are mainly caused by afterslip along the EQ3 fault plane.

Discussion

The role of fault geometry in the separation of multiplet thrust earthquakes

Our results show that within eight days, five strong earthquakes ruptured five, sub-parallel thrust faults, migrating first to the west (in EQ2) and then progressively eastwards (in EQ3, EQ4 and EQ5) for a total fault zone length of about 50 km. Each of the five mainshocks ruptured for 4–10 km along strike, and over a depth range of 2–8 km. Coulomb stress calculations using our preferred five fault model suggest that each mainshock brought parts of the neighbouring segments as much as 0.5–2 MPa closer to failure (see Methods and Fig. S14), a pattern often observed in multiplet sequences[52–56]. However, this does not rule out other potential causes of triggering, such as dynamic stresses[7] or afterslip, nor does it explain the relative timing of the successive earthquakes. To us, a more interesting question is why overall slip is partitioned into five moderate earthquakes rather than one much larger one. Here, we consider whether variable fault geometry may have controlled this rupture segmentation.

Fault geometrical complexities such as bends, step-overs, and gaps, are well known to influence earthquake rupture propagation and arrest[57–61]. An analysis of 67 historical strike-slip ruptures found that fault bends of 25° have a probability of 50% of terminating rupture propagation[61], but the influence of fault bends on thrust-slip propagation is still unclear. Our InSAR derived strikes for EQ1–EQ5 are ~250°, ~275°, ~274°, ~259° and ~243°, respectively, but for inclined faults, bend angles also require consideration of dip. We calculate[62] a ~ 16° fault bend west of EQ1 with EQ2,

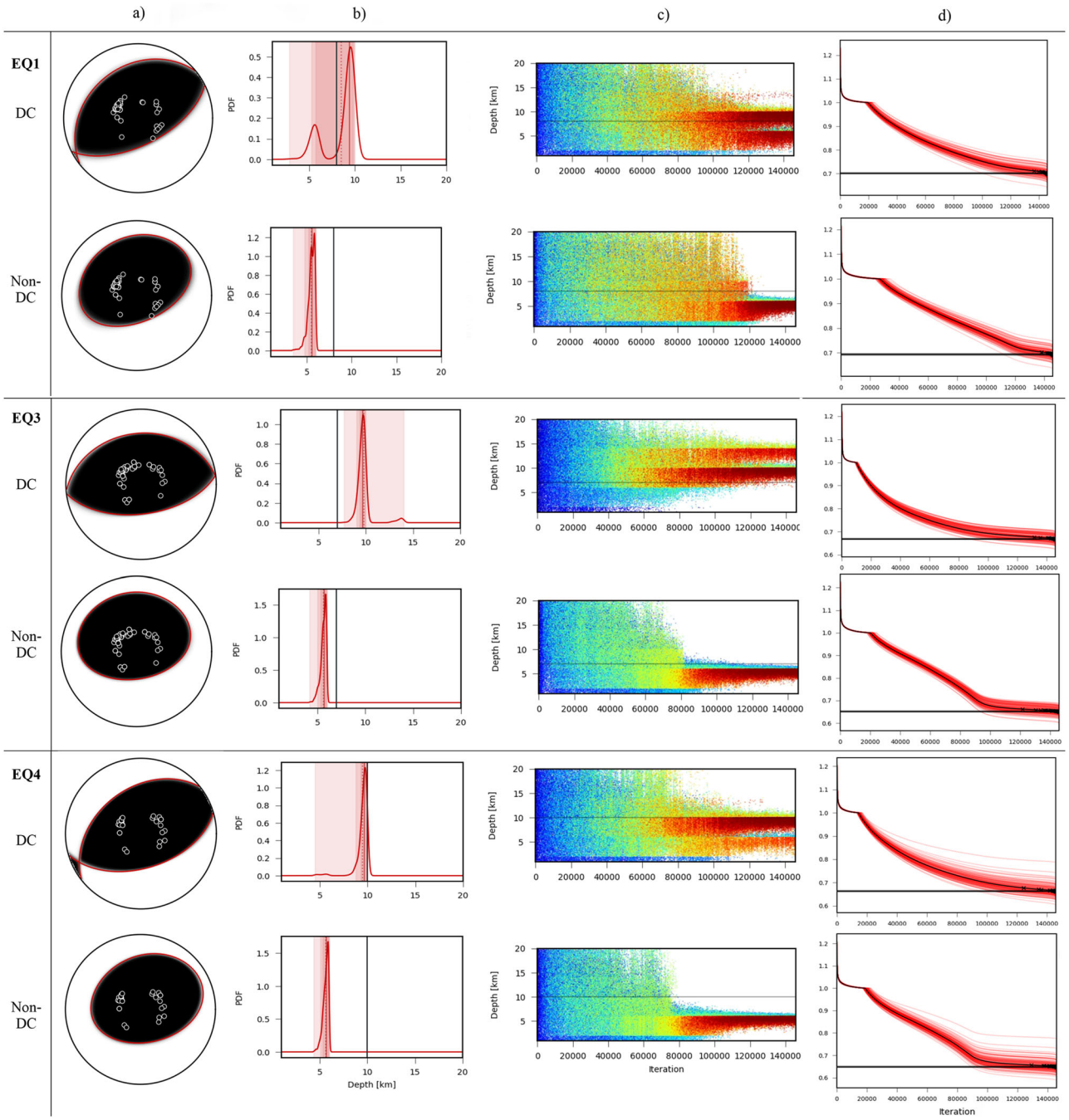

Fig. 6 | Comparison of DC and Non-DC inversions of EQ1 (upper two rows), EQ4 (middle two rows), and EQ5 (lower two rows). a Fuzzy full MT solutions illustrating the uncertainty of each solution, with *P* wave first polarities. **b** Centroid depth probability distribution functions across the 1–20 km model space. The solid and dashed red vertical lines give the median and mean values, respectively, while the pink shaded areas show 90% and 68% confidence intervals (darker shadings) and the range (lightest shading). Dark grey vertical lines show reference centroid depths from GEOFON. **c** The sequence of centroid depths as a function of optimization through 140,000 iterations, coloured by misfit from high (blue) to low (red). **d** The unitless Bootstrap Misfit (y-axis) decreases in bootstrap chains (red lines) through 140,000 iterations (x-axis). This represents the sorted misfit values of individual bootstrap chains, indicating how models are ranked by their misfit in each bootstrap configuration. The black line among the red lines shows the decrease of global misfit value. The horizontal black lines indicate the final misfit values.

a ~ 12° bend east of EQ1 with EQ3, and fault bends of 9°–10° together with step-overs of ~2 km between both EQ3 and EQ4 and EQ4 and the EQ5. These geometric relations suggest that bend angles of ~10° to ~15° might often be sufficient to terminate rupture propagation in thrust belt settings.

We can also compare the Herat earthquakes with seven other similarly well-recorded multiplet sequences involving shallow reverse faulting in continental fold-and-thrust or transpressional belts (Fig. 7). Several of these sequences involve along-strike segmentation similar to the Herat sequence, but the compilation does not reveal a well-defined limiting angle across which thrust earthquakes cease to propagate in the way that there is for strike-slip earthquakes[61]. For example, the first and second earthquakes in the 2017 Hojedk triplet appear separated into distinct ruptures by a bend in fault strike of just 6°, whereas single mainshocks in the 2005–2008 Qeshm, 2008–2009 Qaidam, and 2020 Khalili sequences propagated across greater bends of 40°, 22°, and 13°, respectively[9,15,19,23]. The 1997 Harnai earthquakes differ by 13° in fault strike, though the second mainshock nucleated ~40 km

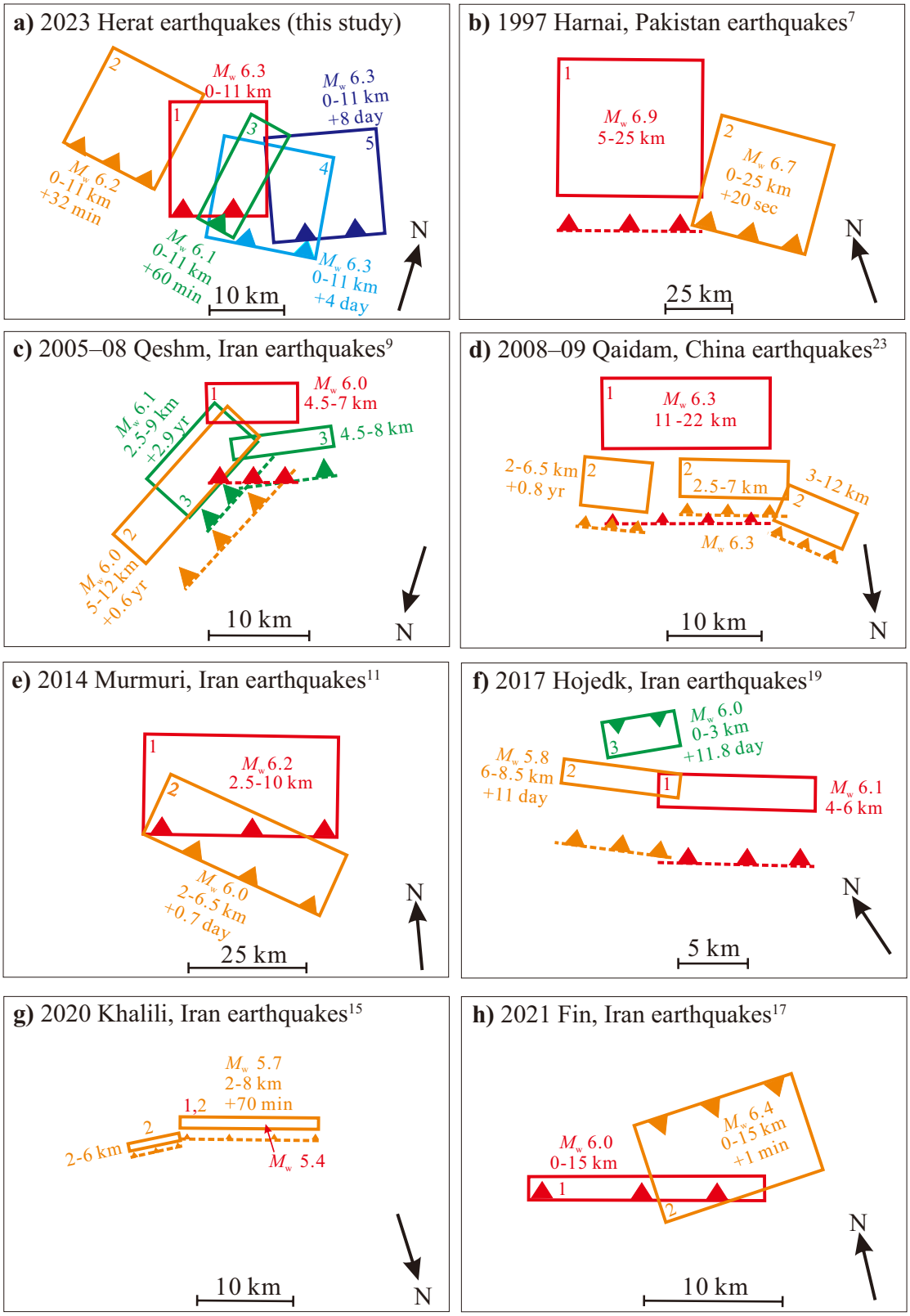

Fig. 7 | Geometic relationships between successive earthquakes in shallow, continental reverse faulting multiplets studied with InSAR. Maps are oriented such that the first earthquake in each sequence (in red) is dipping towards the top of the map; successive earthquakes are also coloured consistently. Dashed lines indicate fault surface projections (for detailed fault parameters, see Table S7) and numbers indicate the magnitude, rupture depth range, and time interval from the initial earthquake.

from the first indicating that the bend played at most a secondary role in rupture segmentation[7]. Moreover, more exotic geometries are also possible: the second earthquake of the 2014 Murmuri sequence ruptured a synthetic thrust in the hanging wall of the first[11]; the 2017 Hojedk and 2021 Fin earthquakes involved antithetic thrust faulting[17,19]; and the 2008–2009 Qaidam doublet involved depth segmentation, with the second earthquake rupturing up-dip of the first[23]. Overall, this shows that there are no simple commonalities in the geometries of thrust multiplet sequences.

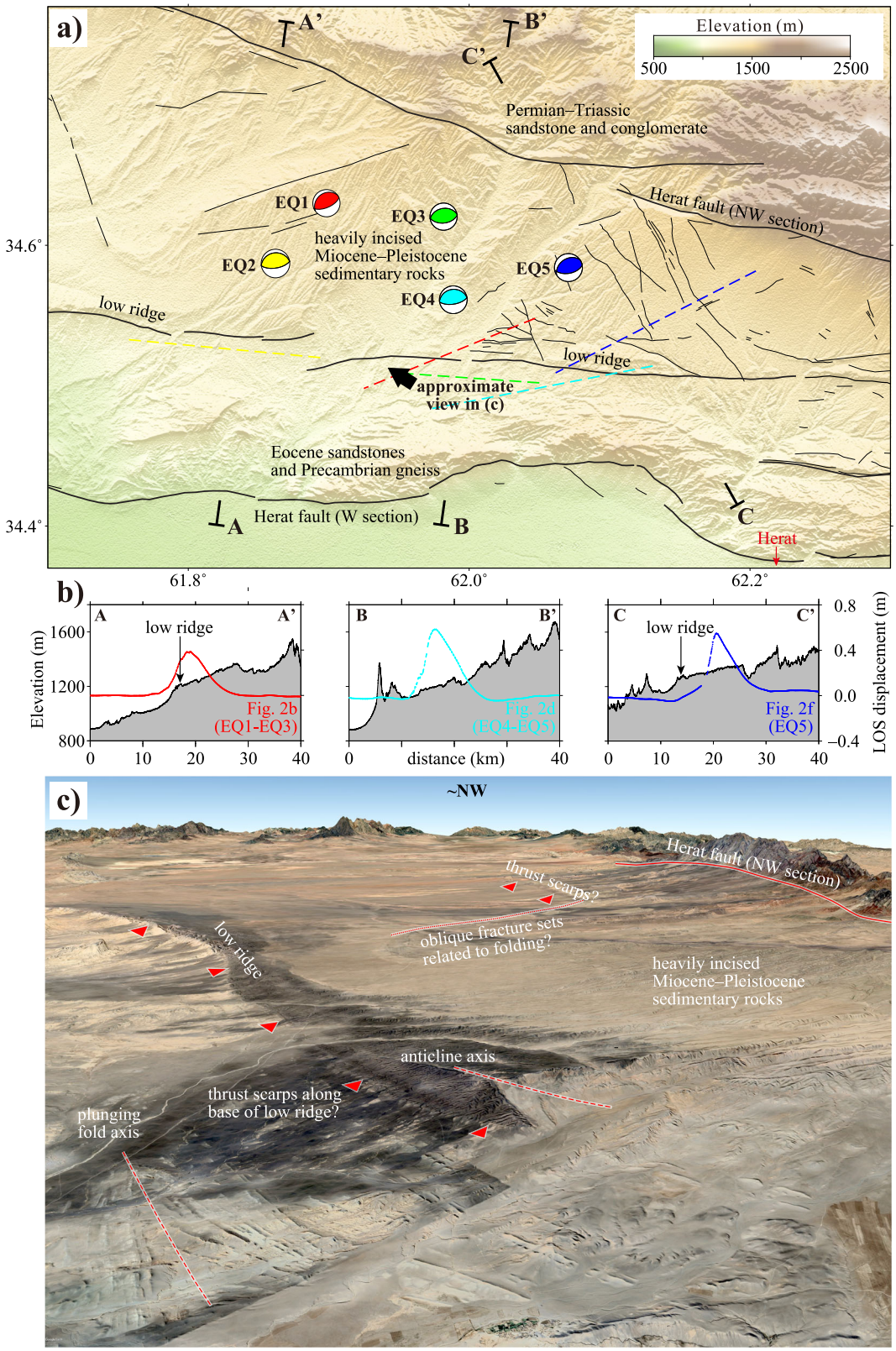

Fig. 8 | Regional faulting and geomorphology. a Revised fault map of the epicentral region. Thin black lines are faults from the USGS[46] while thicker lines are additional faults we mapped ourselves. **b** Cross-sections of topography and InSAR coseismic deformation from the lines A-A', B-B' and C-C' in (**a**). **c** Annotated Google Earth (Image © 2025 Airbus) perspective looking roughly northwestwards across the western part of the epicentral area. There is × 3 vertical exaggeration.

Geomorphology in the epicentral region

Next, we consider the geologic and geomorphic context of the reverse faults that ruptured in the 2023 Herat sequence. These underlie a relatively low-relief region of Neogene clastic sedimentary rocks between the W and NW strands of the Herat fault, that contrast with older bedrock exposed in steeper topography immediately north of either strand (Fig. 8a). Though surface projections of our EQ1–EQ5 model faults do not match any of the scattered faults mapped previously by the USGS[46],

our additional analysis of our Google Earth imagery reveals an abundance of evidence for active N-S shortening in this area. Coseismic deformation is centered on a planar, southward-tilted surface that is heavily incised (Fig. 8b), likely in response to long-term uplift. A low-lying, E-W-trending ridge with a sharp southern flank marks the southern edge of the planar surface, and in one place appears to mark a gentle anticline (Fig. 8c). This anticline ridge parallels the surface projections of the faults responsible for EQ2 and EQ3, is only a little misoriented from the EQ1 and EQ4 faults, and matches the location of the narrow fringe lobe seen in InSAR imagery spanning EQ4 and EQ5 (Fig. 4j, m, p). We therefore interpret it to be the surface expression of at least two and possibly four of the fault segments responsible for the Herat sequence, and that it grew co- and post-seismically due to slip on the underlying thrust faults, patterns seen in analogous regions of neighbouring eastern Iran[63]. Scattered NE- and NW-trending faults mapped north and east of the anticline ridge may represent oblique fracture sets associated with long-term, N-S folding, rather than primary tectonic faults (Fig. 8a, c). The ridge can be traced for ~20 km west of EQ2 and ~15 km east of EQ4, with patterns of river incision and oblique fracture sets observed up to ~50 km further eastwards still, suggesting that only part of a much longer thrust system ruptured in the 2023 sequence. This strongly motivates additional geomorphic and geologic mapping over a much broader area in the future.

Active tectonics in northwestern Afghanistan

The collision of the Arabia and Eurasia plates results in northward motion of central Iran with respect to Eurasia, with velocities decreasing eastward to near zero at the Iran-Afghanistan border[31,64,65]. As such, Afghanistan is often considered a promontory of the stable Eurasia plate[38,39], but the 2023 Herat sequence shows that western Afghanistan is internally deforming below the resolution of the sparse regional GNSS data. The pure, north-dipping thrust faulting yielded by our inversions suggest that northwestern Afghanistan accommodates slow, N-S shortening of the Farah and Helmand blocks (making up western and southern Afghanistan) against the Turan platform in southern Eurasia. The 2023 sequence therefore highlights complex structural branching and slip partitioning at the western terminus of the Herat fault. There may also be a strike-slip component to this motion, and slip-partitioning, if the Herat strike-slip fault is also active at this longitude, but there is no evidence for or against this from the 2023 sequence.

Field mapping suggests that the Herat fault reactivated a steeply-dipping suture zone in the Tertiary[42], but its dip angle is much steeper than those implicated in the 2023 sequence. The thrust faults involved in the 2023 sequence have consistent strikes as those in the easternmost Alborz mountains. Field geological surveys show that the eastern Alborz shares a similar pre-Jurassic structural history with the Paropamisus mountain[66,67]; the two ranges are co-linear but with significantly reduced topography in the intervening region along the Iran–Afghanistan border (Fig. 1b). This region of muted topography may reflect the transition between sinistral transpression along the Doruneh fault in eastern Iran and dextral transpression along the Herat fault system in Afghanistan.

Summary

The 2023 Herat quintuplet earthquakes ruptured five north-dipping thrust faults sequentially along strike, westwards initially, and thereafter eastwards. The faults have consistent, moderate (30–40°) dip angles but variable strikes, from ~WNW in the west to ~ENE in the east. Relatively modest fault bends of ~10–15° and step-overs of ~2 km likely played a role in terminating slip propagation in individual earthquakes. Coseismic slip is concentrated in the depth range of 2–8 km, but there was likely some triggered afterslip on the shallow, up-dip portion of at least one of the faults. The shallow faulting is expressed in the geomorphology as a low-lying anticline ridge, but this was not mapped prior to the earthquake sequence.

Methods

Sentinel-1 C-band InSAR data

We mapped coseismic surface deformation in the 2023 Herat earthquake sequence using seven interferograms constructed from eleven individual Sentinel-1A scenes captured from two ascending and two descending tracks. These were processed in GAMMA software[68] and multilooked with a 10:2 range:azimuth ratio. The 30-arc-second Shuttle Radar Topography Mission (SRTM) Digital Elevation Model (DEM) was used to simulate and correct the topographic phase. We manually masked incoherent parts of the interferogram, likely decorrelated through steep phase gradients and/or strong ground shaking, in order to reduce the impact of unwrapping errors in our subsequent fault modelling (Fig. S15). The interferograms were cleaned using an adaptive filter and unwrapped using the minimum cost flow (MCF) method[69].

InSAR slip modelling

We downsampled the unwrapped interferograms uniformly (Table S2) before employing a two-step inversion strategy to solve first for the mainshock fault geometries and subsequently for their slip distributions. In the first step, we used the Geodetic Bayesian Inversion Software (GBIS) implemented in a Bayesian framework[70] to invert non-linearly for the optimum strike, dip, length, width, depth, strike- and dip-slip components of uniform slip, with their uncertainties, of a rectangular fault plane embedded within a homogeneous elastic half-space. We use open search bounds for strike, dip and rake, and allow for broad ranges of slip, length, width, and depth (Table S3, ranges in parentheses). Finding that all the earthquakes are best fit by a north dipping fault geometry, we then repeated the inversion with a N-dipping constraint on fault strike (Table S3, ranges outside parentheses). In the second step, we extended the model fault by several kilometers along strike and up and down dip, subdivided it into 1 km × 1 km sub-fault patches, and used the steepest descent method[71] to invert linearly for the coseismic slip distribution, allowing for rake angles of 45°–135°. For this second step, we calculated the Green's functions using layered elasticities derived from the Crust 1.0 model[72] (Table S4).

As a further check on the reliability of the coseismic slip models, we employed a Jackknife resampling technique[73]. We randomly selected 40% of the downsampled InSAR data from each dataset and reinverted for the coseismic slip distribution, repeating this process 50 times to calculate the standard deviation of slip for each sub-fault patch. The maximum standard deviations are ~0.03 m, ~0.03 m, ~0.04 m, ~0.1 and ~0.12 m for EQ1, EQ2, EQ3, EQ4, and EQ5, respectively (Fig. S16). These values account for ~2%, ~3%, ~4%, ~5% and ~5% of the coseismic slip, indicating that our models are well constrained by the InSAR observations.

For thrust-slip earthquakes oriented roughly E-W, InSAR line-of-sight displacements are dominated by the vertical component of surface deformation. When such earthquakes are buried, it can therefore be difficult to determine the fault dip direction from "bullseye" InSAR deformation signals without additional constraints such as from GNSS data, subsurface geology, or locally recorded aftershock distributions[8,10], none of which are available here. In order to verify the reliability of our north-dipping fault geometries for EQ1–EQ3, EQ4, and EQ5, we also solved for the best fitting south-dipping faults, and then compared the two sets of models. While the observed EQ1–EQ3 interferograms can be fit well with a south-dipping fault, the thrust-slip component of slip reaches an unreasonable ~13.5 m (Fig. S17). The S-dipping model fault inversion for EQ4 was particularly unstable (Fig. S18), while for EQ5 the thrust-slip component of slip reaches an unreasonable ~40 m (Fig. S19). Collectively, these tests therefore strongly support our favoured interpretation of N-dipping faulting in all five of the Herat mainshocks.

Earthquake relocation

We used the Hypocentroidal Decomposition multiple-earthquake relocation procedure[74] implemented in mloc software[75,76] to determine improved

epicenters for the five October 2023 mainshocks, sixty-two of the best-recorded aftershocks up to December 2023, and fifty-eight background events since 2013. This approach minimizes location biases arising from unknown velocity structures by separating the relocation procedure into two distinct steps. In the first, arrival times reported in the bulletins of the International Seismological Centre (ISC), USGS National Earthquake Information Center (NEIC), the permanent Iranian networks operated by the International Institute for Earthquake Engineering and Seismology (IIEES), the Institute of Geophysics, University of Tehran (UTIG), and the University of Mashad, for all phases at all distances, are inverted to determine cluster vectors that describe the relative location and origin time of each individual event with respect to the geometrical mean of all events (the hypocentroid; Fig. S20). In the second step, the absolute location and origin time of the hypocentroid is determined using only arrival time data at local distances (to 1.1° epicentral distance, Figs. S21–24), which, when added to the cluster vectors, establishes the absolute coordinates of all events. With virtually no local-distance data for the Herat sequence itself, we calibrated the sequence by including in the cluster the well-recorded April 2017 M_w 6.0 Sefid Sang sequence[77], located around 180 km WNW of the Herat sequence in north-eastern Iran (Fig. 1a). While the geographic extent of this cluster is greater than normally considered for the purposes of direct calibration[78], we find that the resulting calibrated relocation places the epicenter of EQ5—the only of the mainshocks to be captured solitarily with InSAR—exactly over the deformation centroid in the Fig. 2f interferogram. As such, our results are nearly indistinguishable from those of an alternative approach, in which the cluster is calibrated indirectly by fitting the pattern of relative locations to the pattern of ruptures derived from InSAR analysis[79,80]. Without close-in stations to provide sensitivity to focal depth, we used a default focal depth of 12 km and a default crustal structure modified from the global ak135 model[81] (Table S5) and developed over many years of doing calibrated relocations in Iran[76]. While this default depth is below the base of the rupture planes imaged with InSAR, by repeating the relocation at a range of default depths we found that there is negligible impact on epicentral accuracy, similar to our experience with other clusters that lack close-in stations[82,83].

Moment tensor inversion

We calculated the focal mechanisms of the five mainshock events using high signal-to-noise ratio seismic records at both teleseismic and regional distances, employing an approach that has been successful in neighboring Iran[15,84]. For EQ1, EQ4 and EQ5, we estimated deviatoric moment tensors through inversion of long-period (10–100 s) teleseismic (30°–80°) P and SH body waves in the time domain (Figs. S9, S25–S28, 29). The occurrence of EQ2 and EQ3 so shortly after EQ1 hinders the proper processing and modeling of their P waves at teleseismic distances, since these overlap the waveform and coda of EQ1. As a result, EQ2 and EQ3 moment tensors were instead determined using regional data in the time and frequency domains (Figs. S25, S26, 27). We used the network of the Iranian Seismological Center plus two Incorporated Research Institutions for Seismology (IRIS) stations, filtered in the frequency band of 0.008–0.03 Hz, the dominant periods of Rayleigh and Love waves at these distances. For all five earthquakes, synthetic seismograms were computed using pre-calculated Green's functions[85]. For the teleseismic waveform inversions of EQ1, EQ4 and EQ5, we used the global ak135 model[81], while for regional waveform inversion of EQ2 and EQ3 we used the same, modified ak135 model as for our multiple-event relocation in "The role of fault geometry in the separation of multiplet thrust earthquakes" (Table S6).

For all five events, we employed the Grond probabilistic earthquake source inversion framework[85]. This utilizes a Bayesian bootstrap approach[86] to explore the entire model space, and delineates model parameters and their relevant uncertainties and trade-offs. The Bayesian bootstrap optimization method initiates the model space exploration by sampling from a uniform distribution within specified parameter bounds. All bootstrap realizations were evaluated in parallel. Based on the performance of the tested models, the proposed distributions for new models were gradually and independently updated for every bootstrap realization until they became smaller[84,87]. For each earthquake, we computed two solutions: firstly a best double couple (DC) approximation parameterized by strike, dip and rake, and secondly a complete, deviatoric non double-couple (non-DC) moment tensor. In each case, we also inverted for centroid time, location, depth, and a duration parameter governing a half-sinusoid-shaped source time function.

Static Coulomb stress changes

Sequential fault rupture is often attributed to Coulomb stress loading, with static stresses arising from slip in one earthquake promoting failure of the next[52–56]. The Coulomb failure criterion is expressed as:

$$\Delta\sigma f = \Delta\tau s - \mu'\Delta\sigma n \quad (1)$$

where $\Delta\sigma_f$ is the Coulomb stress change on a receiver fault resulting from slip on a source fault (positive values indicate receiver faults brought closer to failure), $\Delta\tau_s$ is the shear stress change (positive in the direction of slip), $\Delta\sigma_n$ is the normal stress change (positive when unclamped), and μ' is the effective coefficient of friction[88].

To explore its role in the Herat sequence we used Coulomb 3.3 software[89] to calculate Coulomb stress changes on the 2023 thrust fault segments produced by each successive mainshock. Using our preferred, five segment InSAR slip model as both source faults and receiver fault geometries (Table S1), and taking μ' as 0.4 following precedent[52,90]. we mapped $\Delta\sigma_f$ on each successive fault plane arising from slip in all preceding mainshocks. In other words, we calculated $\Delta\sigma_f$ on the EQ2 fault plane resulting from slip in EQ1, on the EQ3 fault plane resulting from slip in both EQ1 and EQ2, and so on. We find that EQ1 loads the middle eastern portion of the EQ2 fault, with a peak $\Delta\sigma_f$ of ~2 MPa (Fig. S14a). Similarly, the middle-western portion of the EQ3 fault, the northern portion of the EQ4 fault, and the middle-western portion of the EQ5 fault, are located in regions of positive $\Delta\sigma_f$, averaging ~0.5–1.0 MPa (Fig. S14g). Other studies have found that $\Delta\sigma_f$ of just 0.1 MPa can result in receiver fault slip[88,91], hinting at a role for static stress triggering in the Herat sequence. However, when we account for where slip in EQ2–EQ5 actually initiated, the triggering relations are more obscure. Using the same set of source faults, we estimated $\Delta\sigma_f$ at our best estimate of where slip in EQ2–EQ5 initiated, namely our relocated EQ2–EQ5 epicenters and their non-DC centroid depths (Figs. S14b, S14d, S14f, S14h). EQ2, EQ3, EQ4 and EQ5 each initiated close to boundaries between regions of positive and negative $\Delta\sigma_f$. Since these calculations are sensitive to small variations in both source and receiver fault geometry and location, it is therefore unclear whether static stresses played a significant role in triggering each successive rupture.

Data availability

InSAR data were downloaded from the Alaska Satellite Facility (ASF) (https://search.asf.alaska.edu/#/). We used focal mechanisms from the Global Centroid Moment Tensor project (https://www.globalcmt.org/), the U.S. Geological Survey's Comprehensive Earthquake Catalog (https://earthquake.usgs.gov/data/comcat/), and the GEOFON Data Centre (1993) of the GFZ German Research Centre for Geosciences (https://geofon.gfz-potsdam.de/) which are based on data from the GEOFON Extended Virtual Network (GEVN) partner networks. The seismic waveforms of the Iran network were downloaded from the Iranian Seismological Center (http://irsc.ut.ac.ir/), and are freely available for events larger than M 4. Teleseismic waveforms were obtained from the Incorporated Research Institutions for Seismology (IRIS). The interferograms, earthquake relocation and slip model can obtained in https://zenodo.org/records/14736494.

Received: 7 August 2024; Accepted: 7 February 2025;
Published online: 22 February 2025

References

1. Kagan, Y. & Jackson, D. Worldwide doublets of large shallow earthquakes. *Bull. Seismological Soc. Am.* **89**, 1147–1155 (1999).
2. Beavan, J. et al. Near-simultaneous great earthquakes at Tongan megathrust and outer rise in September 2009. *Nature* **466**, 959–963 (2010).
3. Decriem, J. et al. The 2008 May 29 earthquake doublet in SW Iceland. *Geophys. J. Int.* **181**, 1128–1146 (2010).
4. Lay, T. et al. The 2009 Samoa-Tonga great earthquake triggered doublet. *Nature* **466**, 964–968 (2010).
5. Lay, T., Duputel, Z., Ye, L. & Kanamori, H. The December 7, 2012 Japan Trench intraplate doublet (Mw 7.2, 7.1) and interactions between near-trench intraplate thrust and normal faulting. *Phys. Earth Planet. Inter.* **220**, 73–78 (2013).
6. Hicks, S. P. & Rietbrock, A. Seismic slip on an upper-plate normal fault during a large subduction megathrust rupture. *Nat. Geosci.* **8**, 955–960 (2015).
7. Nissen, E. et al. Limitations of rupture forecasting exposed by instantaneously triggered earthquake doublet. *Nat. Geosci.* **9**, 330–336 (2016).
8. Lohman, R. B. & Barnhart, W. D. Evaluation of earthquake triggering during the 2005–2008 earthquake sequence on Qeshm Island, Iran. *J. Geophys. Res.: Solid Earth* **115**, 2010JB007710 (2010).
9. Nissen, E. et al. The vertical separation of mainshock rupture and microseismicity at Qeshm island in the Zagros fold-and-thrust belt, Iran. *Earth Planet. Sci. Lett.* **296**, 181–194 (2010).
10. Roustaei, M. et al. The 2006 March 25 Fin earthquakes (Iran)-insights into the vertical extents of faulting in the Zagros Simply Folded Belt. Geophys. J. Int. https://doi.org/10.1111/j.1365-246X.2010.04601.x (2010).
11. Copley, A. et al. Seismogenic faulting of the sedimentary sequence and laterally variable material properties in the Zagros Mountains (Iran) revealed by the August 2014 Murmuri (E. Dehloran) earthquake sequence. *Geophys. J. Int.* **203**, 1436–1459 (2015).
12. Motagh, M. et al. The 18 August 2014 Mw 6.2 Mormori, Iran, Earthquake: A Thin-Skinned Faulting in the Zagros Mountain Inferred from InSAR Measurements. *Seismological Res. Lett.* **86**, 775–782 (2015).
13. Kintner, J. A., Wauthier, C. & Ammon, C. J. InSAR and seismic analyses of the 2014–15 earthquake sequence near Bushkan, Iran: shallow faulting in the core of an anticline fold. *Geophys. J. Int.* **217**, 1011–1023 (2019).
14. Nissen, E. et al. The 12 November 2017 *Mw* 7.3 Ezgeleh-Sarpolzahab (Iran) Earthquake and Active Tectonics of the Lurestan Arc. *J. Geophys. Res.: Solid Earth* **124**, 2124–2152 (2019).
15. Jamalreyhani, M. et al. The 2019–2020 Khalili (Iran) Earthquake Sequence—Anthropogenic Seismicity in the Zagros Simply Folded Belt? *J. Geophys. Res.: Solid Earth* **126**, e2021JB022797 (2021).
16. Rezapour, M. & Jamalreyhani, M. R. Source fault analyses from InSAR data and aftershocks for the Fin doublet earthquakes on 14 November 2021 in Hormozgan province, South Iran. *J. Earth Space Phys.* https://doi.org/10.22059/jesphys.2022.337959.1007399 (2022).
17. Golshadi, Z. et al. Contemporaneous Thick-and Thin-Skinned Seismotectonics in the External Zagros: The Case of the 2021 Fin Doublet, Iran. *Remote Sens.* **15**, 2981 (2023).
18. Yang, Y. et al. The 2022 Hormozgan Doublet Earthquake: Two Blind Thrusts-Related Folding in Zagros Fold-And-Thrust Belt, Southeast Iran. *Geophys. Res. Lett.* **50**, e2022GL101902 (2023).
19. Savidge, E. et al. The December 2017 Hojedk (Iran) earthquake triplet—sequential rupture of shallow reverse faults in a strike-slip restraining bend. *Geophys. J. Int.* **217**, 909–925 (2019).
20. McNab, F., Sloan, R. & Walker, R. Simultaneous orthogonal shortening in the Afghan-Tajik Depression. *Geology* **47**, 862–866 (2019).
21. Pinel-Puysségur, B., Grandin, R., Bollinger, L. & Baudry, C. Multifaulting in a tectonic syntaxis revealed by InSAR: The case of the Ziarat earthquake sequence (Pakistan). *J. Geophys. Res.: Solid Earth* **119**, 5838–5854 (2014).
22. Sloan, R. A., Jackson, J. A., McKenzie, D. & Priestley, K. Earthquake depth distributions in central Asia, and their relations with lithosphere thickness, shortening and extension: Earthquake depth distributions in central Asia. *Geophys. J. Int.* **185**, 1–29 (2011).
23. Elliott, J. R. et al. Depth segmentation of the seismogenic continental crust: The 2008 and 2009 Qaidam earthquakes. *Geophys. Res. Lett.* **38**, L06305 (2011).
24. Choy, G. L. & Boatwright, J. Teleseismic and near-field analysis of the Nahanni earthquakes in the Northwest Territories, Canada. *Bull. Seismol. Soc. Am.* **78**, 1627–1652 (1988).
25. Weston, J., Ferreira, A. M. G. & Funning, G. J. Global compilation of interferometric synthetic aperture radar earthquake source models: 1. Comparisons with seismic catalogs. *J. Geophys. Res.: Solid Earth* **116**, B08408 (2011).
26. Molnar, P. & Lyon-Caen, H. Fault plane solutions of earthquakes and active tectonics of the Tibetan Plateau and its margins. *Geophys. J. Int.* **99**, 123–153 (1989).
27. Maggi, A., Jackson, J. A., Priestley, K. & Baker, C. A re-assessment of focal depth distributions in southern Iran, the Tien Shan and northern India: Do earthquakes really occur in the continental mantle? *Geophys. J. Int.* **143**, 629–661 (2000).
28. Engdahl, E. R., Jackson, J. A., Myers, S. C., Bergman, E. A. & Priestley, K. Relocation and assessment of seismicity in the Iran region. *Geophys. J. Int.* **167**, 761–778 (2006).
29. Wimpenny, S. & Watson, C. S. gWFM: A global catalog of moderate-magnitude earthquakes studied using teleseismic body waves. *Seismol. Res. Lett.* **92**, 212–226 (2021).
30. Penney, C. et al. Megathrust and accretionary wedge properties and behaviour in the Makran subduction zone. *Geophys. J. Int.* **209**, 1800–1830 (2017).
31. Vernant, P. et al. Present-day crustal deformation and plate kinematics in the Middle East constrained by GPS measurements in Iran and northern Oman. *Geophys. J. Int.* **157**, 381–398 (2004).
32. Walker, R. & Jackson, J. Active tectonics and late Cenozoic strain distribution in central and eastern Iran. *Tectonics* **23**, 2003TC001529 (2004).
33. Lawrence, R. D., Yeats, R. S., Khan, S. H., Farah, A. & DeJong, K. A. Thrust and strike slip fault interaction along the Chaman transform zone. *Pak. Geol. Soc., Lond., Spec. Publ.* **9**, 363–370 (1981).
34. Szeliga, W., Bilham, R., Kakar, D. M. & Lodi, S. H. Interseismic strain accumulation along the western boundary of the Indian subcontinent. *J. Geophys. Res.: Solid Earth* **117**, B08404 (2012).
35. Dalaison, M, Jolivet, R. & Le Pourhiet, L. A snapshot of the long-term evolution of a distributed tectonic plate boundary. *Sci. Adv.* **9**, eadd7235 (2023).
36. Kufner, S. K. et al. Deep India meets deep Asia: Lithospheric indentation, delamination and break-off under Pamir and Hindu Kush (Central Asia). *Earth Planet. Sci. Lett.* **435**, 171–184 (2016).
37. Ambraseys, N. & Bilham, R. The Tectonic Setting of Bamiyan and Seismicity in and Near Afghanistan for the Past Twelve Centuries. in *After the Destruction of Giant Buddha Statues in Bamiyan (Afghanistan) in 2001* (ed. Margottini, C.) 101–152 (Springer Berlin Heidelberg, Berlin, Heidelberg, 2014). https://doi.org/10.1007/978-3-642-30051-6_6.
38. Jackson, J. & McKenzie, D. Active tectonics of the Alpine—Himalayan Belt between western Turkey and Pakistan. *Geophys. J. Int.* **77**, 185–264 (1984).
39. Hollingsworth, J. et al. Oroclinal bending, distributed thrust and strike-slip faulting, and the accommodation of Arabia-Eurasia convergence in NE Iran since the Oligocene: Thrust and strike-slip faulting in NE Iran. *Geophys. J. Int.* **181**, 1214–1246 (2010).

40. Wellman, H. W. Active wrench faults of Iran, Afghanistan and Pakistan. *Geologische Rundsch.* **55**, 716–735 (1966).
41. Sborshchikov, I. M., Savostin, L. A. & Zonenshain, L. P. Present plate tectonics between Turkey and Tibet. *Tectonophysics* **79**, 45–73 (1981).
42. Tapponnier, P., Mattauer, M., Proust, F. & Cassaigneau, C. Mesozoic ophiolites, sutures, and large-scale tectonic movements in Afghanistan. *Earth Planet. Sci. Lett.* **52**, 355–371 (1981).
43. Ambraseys, N. N. & Melville, C. P. *A History of Persian Earthquakes*. (Cambridge University Press, 2005).
44. Ambraseys, N. & Bilham, R. Earthquakes in afghanistan. *Seismological Res. Lett.* **74**, 107–123 (2003).
45. Brookfield, M. E. & Hashmat, A. The geology and petroleum potential of the North Afghan platform and adjacent areas (northern Afghanistan, with parts of southern Turkmenistan, Uzbekistan and Tajikistan). *Earth-Sci. Rev.* **55**, 41–71 (2001).
46. Ruleman, C. A., Crone, A. J., Machette, M. N., Haller, K. M. & Rukstales, K. S. Map and Database of Probable and Possible Quaternary Faults in Afghanistan. *USGS Open-File Report*, https://doi.org/10.3133/ofr20071103 (2007).
47. Shnizai, Z. Mapping of active and presumed active faults in Afghanistan by interpretation of 1-arcsecond SRTM anaglyph images. *J. Seismol.* **24**, 1131–1157 (2020).
48. Doebrich, J. L. et al. *Geologic and Mineral Resource Map of Afghanistan*. US Geological Survey (2006).
49. Jónsson, S., Zebker, H., Segall, P. & Amelung, F. Fault Slip Distribution of the 1999 Mw 7.1 Hector Mine, California, Earthquake, Estimated from Satellite Radar and GPS Measurements. *Bull. Seismological Soc. Am.* **92**, 1377–1389 (2002).
50. Santos, E. T. F. & Bassrei, A. L- and Θ-curve approaches for the selection of regularization parameter in geophysical diffraction tomography. *Computers Geosci.* **33**, 618–629 (2007).
51. Cesca, S. et al. Complex rupture process of the Mw 7.8, 2016, Kaikoura earthquake, New Zealand, and its aftershock sequence. *Earth Planet. Sci. Lett.* **478**, 110–120 (2017).
52. King, G. C. P. & Cocco, M. Fault interaction by elastic stress changes: New clues from earthquake sequences. in *Advances in Geophysics* (eds. Dmowska, R. & Saltzman, B.) 44 1–VIII (2001).
53. Martínez-Díaz, J. J. et al. Tectonic and seismic implications of an intersegment rupture. *Tectonophysics* **546–547**, 28–37 (2012).
54. Wang, L., Gao, H., Feng, G. & Xu, W. Source parameters and triggering links of the earthquake sequence in central Italy from 2009 to 2016 analyzed with GPS and InSAR data. *Tectonophysics* **744**, 285–295 (2018).
55. Zhao, D. et al. InSAR and GPS derived coseismic deformation and fault model of the 2017 Ms 7.0 Jiuzhaigou earthquake in the Northeast Bayanhar block. *Tectonophysics* **726**, 86–99 (2018).
56. Zhao, L. et al. Coseismic deformation and multi-fault slip model of the 2019 Mindanao earthquake sequence derived from Sentinel-1 and ALOS-2 data. *Tectonophysics* **799**, 228707 (2021).
57. Wesnousky, S. G. Displacement and Geometrical Characteristics of Earthquake Surface Ruptures: Issues and Implications for Seismic-Hazard Analysis and the Process of Earthquake Rupture. *Bull. Seismological Soc. Am.* **98**, 1609–1632 (2008).
58. Wesnousky, S. G. Predicting the endpoints of earthquake ruptures. *Nature* **444**, 358–360 (2006).
59. Zhao, L. et al. Fault geometry and low frictional control of the near-field postseismic deformation of the 2021 Mw 7.3 Maduo earthquake. *Tectonophysics* **863**, 230000 (2023).
60. Zhang, Y. et al. Geometric controls on cascading rupture of the 2023 Kahramanmaraş earthquake doublet. *Nat. Geosci.* **16**, 1054–1060 (2023).
61. Biasi, G. P. & Wesnousky, S. G. Bends and ends of surface ruptures. *Bull. Seismological Soc. Am.* **107**, 2543–2560 (2017).
62. Allmendinger, R. W., Siron, C. R. & Scott, C. P. Structural data collection with mobile devices: Accuracy, redundancy, and best practices. *J. Struct. Geol.* **102**, 98–112 (2017).
63. Copley, A. & Reynolds, K. Imaging topographic growth by long-lived postseismic afterslip at Sefidabeh, east Iran. *Tectonics* **33**, 330–345 (2014).
64. Khorrami, F. et al. An up-to-date crustal deformation map of Iran using integrated campaign-mode and permanent GPS velocities. *Geophys. J. Int.* **217**, 832–843 (2019).
65. Mousavi, Z. et al. Global Positioning System constraints on the active tectonics of NE Iran and the South Caspian region. *Earth Planet. Sci. Lett.* **377–378**, 287–298 (2013).
66. Golonka, J. Plate tectonic evolution of the southern margin of Eurasia in the Mesozoic and Cenozoic. *Tectonophysics* **381**, 235–273 (2004).
67. Natal'in, B. A. & Şengör, A. M. C. Late Palaeozoic to Triassic evolution of the Turan and Scythian platforms: The pre-history of the Palaeo-Tethyan closure. *Tectonophysics* **404**, 175–202 (2005).
68. Wegnüller, U. et al. Sentinel-1 Support in the GAMMA Software. *Procedia Computer Sci.* **100**, 1305–1312 (2016).
69. Goldstein, R. M. & Werner, C. L. Radar interferogram filtering for geophysical applications. *Geophys. Res. Lett.* **25**, 4035–4038 (1998).
70. Bagnardi, M. & Hooper, A. Inversion of Surface Deformation Data for Rapid Estimates of Source Parameters and Uncertainties: A Bayesian Approach. *Geochem. Geophysics Geosystems* **19**, 2194–2211 (2018).
71. Wang, R. et al. The 2011 Mw 9.0 Tohoku Earthquake: Comparison of GPS and Strong-Motion Data. *Bull. Seismological Soc. Am.* **103**, 1336–1347 (2013).
72. Bevis, M., Pan, E., Zhou, H., Han, F. & Zhu, R. Surface Deformation due to Loading of a Layered Elastic Half-space: Constructing the Solution for a General Polygonal Load. *Acta Geophysica* **63**, 957–977 (2015).
73. Melgar, D. et al. Seismogeodesy of the 2014 *Mw* 6.1 Napa earthquake, California: Rapid response and modeling of fast rupture on a dipping strike-slip fault. *J. Geophys. Res.: Solid Earth* **120**, 5013–5033 (2015).
74. Jordan, T. & Sverdrup, K. Teleseismic location techniques and their application to earthquake clusters in the South-Central Pacific. *Bull. Seismological Soc. Am.* **71**, 1105–1130 (1981).
75. Bergman, E. A. & Solomon, S. C. Earthquake swarms on the Mid-Atlantic Ridge: Products of magmatism or extensional tectonics? *J. Geophys. Res.: Solid Earth* **95**, 4943–4965 (1990).
76. Bergman, E. A. et al. A global catalog of calibrated earthquake locations. *Seismological Res. Lett.* **94**, 485–495 (2023).
77. Aflaki, M. et al. The 2017 Mw 6 Sefid Sang earthquake and its implication for the geodynamics of NE Iran. *Geophys. J. Int.* **218**, 1227–1245 (2019).
78. Karasözen, E., Nissen, E., Bergman, E. A. & Ghods, A. Seismotectonics of the Zagros (Iran) From Orogen-Wide, Calibrated Earthquake Relocations. *J. Geophys. Res.: Solid Earth* **124**, 9109–9129 (2019).
79. Walker, R. T. et al. The 2010–2011 South Rigan (Baluchestan) earthquake sequence and its implications for distributed deformation and earthquake hazard in southeast Iran. *Geophys. J. Int.* **193**, 349–374 (2013).
80. Walker, R. T., Bergman, E. A., Szeliga, W. & Fielding, E. J. Insights into the 1968-1997 Dasht-e-Bayaz and Zirkuh earthquake sequences, eastern Iran, from calibrated relocations, InSAR and high-resolution satellite imagery: Dasht-e-Bayaz and Zirkuh earthquake sequences. *Geophys. J. Int.* **187**, 1577–1603 (2011).
81. Kennett, B. L. N., Engdahl, E. R. & Buland, R. Constraints on seismic velocities in the Earth from traveltimes. *Geophys. J. Int.* **122**, 108–124 (1995).
82. Ghods, A., Rezapour, M., Bergman, E., Mortezanejad, G. & Talebian, M. Relocation of the 2006 Mw 6.1 Silakhour, Iran, earthquake

sequence: details of fault segmentation on the main recent fault. *Bull. Seismological Soc. Am.* **102**, 398–416 (2012).
83. Karasözen, E., Nissen, E., Bergman, E. A., Johnson, K. L. & Walters, R. J. Normal faulting in the Simav graben of western Turkey reassessed with calibrated earthquake relocations. *J. Geophys. Res.: Solid Earth* **121**, 4553–4574 (2016).
84. Jamalreyhani, M. et al. Insight into the 2017–2019 Lurestan arc seismic sequence (Zagros, Iran); complex earthquake interaction in the basement and sediments. *Geophys. J. Int.* **230**, 114–130 (2022).
85. Heimann, S. et al. Grond: A probabilistic earthquake source inversion framework. *Potsdam: GFZ Data Services*, https://doi.org/10.5880/GFZ.2.1.2018.003 (2018).
86. Heimann, S. *A robust method to estimate kinematic earthquake source parameters*. PhD dissertation, Staats-und Universitätsbibliothek Hamburg Carl von Ossietzky (2011).
87. Kühn, D., Heimann, S., Isken, M. P., Ruigrok, E. & Dost, B. Probabilistic Moment Tensor Inversion for Hydrocarbon-Induced Seismicity in the Groningen Gas Field, The Netherlands, Part 1: Testing. *Bull. Seismological Soc. Am.* **110**, 2095–2111 (2020).
88. King, G. C., Stein, R. S. & Lin, J. Static stress changes and the triggering of earthquakes. *Bull. Seismological Soc. Am.* **84**, 935–953 (1994).
89. Toda, S., Stein, R. S., Sevilgen, V. & Lin, J., Coulomb 3.3 Graphic-rich deformation and stress-change software for earthquake, tectonic, and volcano research and teaching—user guide. *US Geological Survey open-file report* 2011-1060 (2011).
90. Yumul, G. P. Jr Westward younging disposition of Philippine ophiolites and its implication for arc evolution. *Isl. Arc* **16**, 306–317 (2007).
91. Toda, S., Stein, R. S., Richards-Dinger, K. & Bozkurt, S. B. Forecasting the evolution of seismicity in southern California: Animations built on earthquake stress transfer. *J. Geophys. Res.: Solid Earth* **110**, B05S16 (2005).
92. Styron, R. & Pagani, M. The GEM Global Active Faults Database. *Earthq. Spectra* **36**, 160–180 (2020).
93. Ischuk, A. et al. Kinematics of the Pamir and Hindu Kush regions from GPS geodesy. *J. Geophys. Res.: Solid Earth* **118**, 2408–2416 (2013).

Acknowledgements

We are grateful to James Jackson and two anonymous reviewers for comments that greatly improved the manuscript. We thank Chengyuan Bai for helping processing InSAR data, and Theron Finley and Zhidan Chen for assisting with geomorphology interpretation. The figures were prepared using the public domain Generic Mapping Tools, MATLAB and Google Earth. This research was supported by the National Natural Science Foundation of China (42388102, 42174023, 42304037), National Science Fund for Distinguished Young Scholars (41925016), National Key Research and Development Program (2022YFB3903602), Natural Science Foundation of Hunan Province (2024JJ3031), Graduate Innovation Project. L.Z. is supported by a scholarship from the China Scholarship Council. E.N. is supported by a Discovery Grant from the Natural Sciences and Engineering Research Council of Canada and a Canada Research Chair.

Author contributions

L.Z., W.X., E.N., and D.Z. conducted the study and wrote the manuscript with contributions from all other coauthors. L.Z., M.J., L.X., and E.A.B. processed the source data. All authors contributed to the discussion and interpretation of the results.

Competing interests

The authors declare no competing interests.

Additional information

Supplementary information The online version contains supplementary material available at https://doi.org/10.1038/s43247-025-02113-7.

Correspondence and requests for materials should be addressed to Wenbin Xu.

Peer review information *Communications Earth & Environment* thanks Manon Dalaison and the other, anonymous, reviewer(s) for their contribution to the peer review of this work. Primary Handling Editor: Joe Aslin. A peer review file is available.